Calibration of misalignment errors in composite waveplates using Mueller matrix ellipsometry

Honggang Gu, Shiyuan Liu, Xiuguo Chen, and Chuanwei Zhang*

State Key Laboratory of Digital Manufacturing Equipment and Technology, Huazhong University of Science and Technology, Wuhan 430074, China

*Corresponding author: chuanweizhang@hust.edu.cn

Received 4 September 2014; revised 27 November 2014; accepted 3 December 2014; posted 9 December 2014 (Doc. ID 222447); published 23 January 2015

Composite waveplates consisting of two or more single waveplates are widely used in optical instruments, such as ellipsometry, polarimetry, cryptography, and photoelasticity. Accurate calibration of the misalignment errors in composite waveplates is of great importance (to minimize or correct the spurious artifacts in the final collected spectral data of these instruments induced by the misalignment errors). In this paper, we choose the fast axis azimuth and the rotary angle of composite waveplates as the detected characteristic parameters to calibrate the misalignment errors in composite waveplates. We first derive a general analytical model to describe the relationship between the mislignment errors and the characteristic parameters, and then propose an inverse approach to the calibration of the misalignment errors in composite waveplates. An experimental device based on the dual rotating-compensator Mueller matrix ellipsometry principle is set up to measure the characteristic parameters of composite waveplates. Both numerical simulations and experiments on an MgF_2–MgF_2–quartz triplate demonstrate the correctness and efficiency of the proposed approach. It is expected that the proposed approach can be readily extended to calibrate the misalignment errors in more complex composite waveplates.

OCIS codes: (120.2130) Ellipsometry and polarimetry; (230.5440) Polarization-selective devices; (220.1140) Alignment; (260.1440) Birefringence; (120.0120) Instrumentation, measurement, and metrology.

http://dx.doi.org/10.1364/AO.54.000684

1. Introduction

Waveplates that are usually made from birefringent materials are widely used to modify the polarization states of polarized light by producing a phase shift between the two orthogonal polarization components [1]. They play an important role in many optical instruments, such as ellipsometry [2,3], polarimetry [4], cryptography [5], and photoelasticity [6]. With the increasing application requirements of achromatic waveplates in a broad band, it is common practice to combine two or more single waveplates into a composite waveplate [7–10]. During fabrication of composite waveplates, alignment of the individual single waveplates is a key procedure to ensure that the fast axes are oriented at appropriate angles with respect to each other. In practice, the alignment procedure inevitably has errors due to the limited precision of the employed alignment systems. These misalignment errors introduce oscillations in the spectra of the polarization properties of composite waveplates, such as the retardance and retardance orientation [11], and furthermore will lead to spurious artifacts in the final collected spectral data of the instruments using such waveplates [12–15]. It is therefore of great importance to accurately calibrate the misalignment errors in composite waveplates in order to minimize or correct the spurious artifacts in the collected spectral data.

1559-128X/15/040684-10$15.00/0

Several methods have been proposed in the published literature to calibrate or identify the misalignment errors in composite waveplates. Most of these methods can be summarized as choosing a group of characteristic parameters that are sensitive to the variation of the misalignment errors in composite waveplates, and then controlling these parameters to achieve the minimal misalignment errors or identify the misalignment errors. For example, the azimuths of the polarizer and analyzer of a polarizer-compensator-analyzer (PCA) ellipsometer in a straight-through mode were chosen in [16] as the characteristic parameter for calibrating the misalignment errors in an optically active biplate. The ellipsometric angles (i.e., the amplitude ratio Ψ_C and the retardance δ_C) were selected in [17] as the characteristic parameters for calibrating the misalignment errors in an MgF_2 biplate using a rotating-analyzer ellipsometer. The angular direction of the neutral axes was chosen as the detected characteristic parameter in [18] for identifying the misalignment errors in an achromatic biplate using a dichotomous method of null intensity. The reported methods can work efficiently in calibrating misalignment errors in simple composite waveplates such as biplates. However, an analytical model for describing the relationship between the misalignment errors and the characteristic parameters was not given in [16,17], and the misalignment errors in biplates were calibrated qualitatively by reducing the oscillations in the chosen characteristic parameters below the limits of detectability [16,17]. Although a theoretical model was derived in [18] for a double-crystal waveplate based on eigenpolarization modes and identifying the misalignment error in the biplate, it is difficult to distinguish the misalignment errors when the composite waveplate consists of more than two single waveplates and contains more than one misalignment error. Thus most of these published methods are not suitable for application to misalignment error calibration in much more complex composite waveplates, due to the lack of a general analytical model to describe the relationship between the misalignment errors and the characteristic parameters of composite waveplates. To the best of our knowledge, no existing method for the quantitative calibration of the misalignment errors in a general composite waveplate has been reported.

In this paper, we aim at quantitatively calibrating the misalignment errors of the fast axes in an arbitrary composite waveplate. We first derive a general analytical model to describe the relationship between the misalignment errors and the characteristic parameters of composite waveplates based on Jones' equivalent theorem [19]. In general, the relationship between the misalignment errors and the characteristic parameters is nonlinear. Thus we further propose an inverse approach to calibrate the misalignment errors in composite waveplates. In order to obtain all of these characteristic parameters of composite waveplates, we set up an experimental device based on dual rotating-compensator Mueller matrix ellipsometry (MME). Both the numerical simulations and the experimental results confirm the correctness and efficiency of the proposed approach to the calibration of misalignment errors in composite waveplates.

The remainder of this paper is organized as follows: Section 2 first derives a general analytical model of composite waveplates, and then proposes an inverse approach to the calibration of the misalignment errors in composite waveplates. Section 3 gives a triplate as an example and shows the numerical simulations to show the effects of the misalignment errors on the triplate, as well as the inverse calibration of the misalignment errors in the triplate. Section 4 presents the experimental setup and the experimental results are discussed. Finally, we draw some conclusions in Section 5.

2. Theory

A. Forward Modeling of Composite Waveplates

According to Jones' theorem, the effect of a waveplate on polarized light can be represented by a 2×2 matrix calculus famously known as the Jones matrix [19]. We consider that the waveplate is arranged in a Cartesian coordinate system, and the light propagates along the z axis and perpendicularly to the plane of the waveplate. The Jones matrix $\mathbf{J}$ of the waveplate (the fast axis of which coincides with the x axis) can be expressed by

$$\mathbf{J}(\delta) = \begin{bmatrix} e^{i\delta/2} & 0 \\ 0 & e^{-i\delta/2} \end{bmatrix}, \tag{1}$$

where δ is the retardance of the waveplate and can be calculated by

$$\delta = 2\pi(n_e - n_o)d/\lambda, \tag{2}$$

where d is the thickness of the waveplate, λ is the wavelength of light passing through the waveplate, and $n_e - n_o$) is the birefringence of the material of the waveplate.

If the fast axis of the waveplate is not lined up with the x axis (in other words, if there is an angle θ between the fast axis and the x axis), the Jones rotation matrix can be used to describe the fast axis azimuth of the waveplate, as shown in Eq. (3):

$$\mathbf{R}(\theta) = \begin{bmatrix} \cos\theta & -\sin\theta \\ \sin\theta & \cos\theta \end{bmatrix}. \tag{3}$$

Taking the fast axis azimuth into account, the Jones matrix of the waveplate can be modified by

$$\mathbf{J}(\delta,\theta)=\mathbf{R}(\theta)\mathbf{J}(\delta)\mathbf{R}(-\theta)$$
$$=\begin{bmatrix}\cos(\delta/2)+i\sin(\delta/2)\cos 2\theta & i\sin(\delta/2)\sin 2\theta\\ i\sin(\delta/2)\sin 2\theta & \cos(\delta/2)-i\sin(\delta/2)\cos 2\theta\end{bmatrix}. \tag{4}$$

The Jones matrix can be represented by the matrix set $\{\boldsymbol{\sigma}_0,\boldsymbol{\sigma}_1,\boldsymbol{\sigma}_2,\boldsymbol{\sigma}_3\}$ combining the unit matrix and the Pauli spin matrices as shown in Eq. (5) [20]:

$$\boldsymbol{\sigma}_0=\begin{bmatrix}1 & 0\\ 0 & 1\end{bmatrix},\quad \boldsymbol{\sigma}_1=\begin{bmatrix}1 & 0\\ 0 & -1\end{bmatrix},$$
$$\boldsymbol{\sigma}_2=\begin{bmatrix}0 & 1\\ 1 & 0\end{bmatrix},\quad \boldsymbol{\sigma}_3=\begin{bmatrix}0 & -i\\ i & 0\end{bmatrix}. \tag{5}$$

It is obvious that the matrix set $\{\boldsymbol{\sigma}_0,\boldsymbol{\sigma}_1,\boldsymbol{\sigma}_2,\boldsymbol{\sigma}_3\}$ is orthogonal and complete, and therefore can be used as a basis for the Jones matrix [10]. Equation (4) can be rewritten as

$$\mathbf{J}(\delta,\theta)=\cos(\delta/2)\cdot\boldsymbol{\sigma}_0+i\,\sin(\delta/2)\cos 2\theta\cdot\boldsymbol{\sigma}_1 + i\,\sin(\delta/2)\sin 2\theta\cdot\boldsymbol{\sigma}_2. \tag{6}$$

It can be seen from Eq. (6) that there will not be $\boldsymbol{\sigma}_3$ in the Jones matrix of a pure waveplate.

A composite waveplate can be treated as an optical system consisting of two or more single waveplates. Again we arrange the optical system in the Cartesian coordinate system, and the light propagates along the z axis and perpendicular to the plane of the waveplate. The component waveplates are numbered as 1, 2,..., n in the order that the light passes through them. Furthermore, let $(d_i,\Delta\theta_i,\alpha_i)$ denote the thickness of the ith waveplate, the designed angle between the fast axis of the ith waveplate and that of the first waveplate, and the misalignment error of the ith waveplate, respectively. The retardance of the ith waveplate δ_i can be calculated by Eq. (2), and the fast axis azimuth of the ith waveplate with respect to the x axis can be presented as $\theta_i=\theta_1+\Delta\theta_i+\alpha_i$. Thus the effect of the composite waveplate on the polarized light can be expressed by

$$\mathbf{U}(\boldsymbol{\alpha},\mathbf{d},\boldsymbol{\Delta\theta},\theta_1)=\mathbf{J}(\delta_n,\theta_n)\cdots\mathbf{J}(\delta_2,\theta_2)\mathbf{J}(\delta_1,\theta_1), \tag{7}$$

where $\boldsymbol{\alpha}=(\alpha_2,\ldots,\alpha_n)$, $\mathbf{d}=(d_1,d_2,\ldots,d_n)$, and $\boldsymbol{\Delta\theta}=(\Delta\theta_2,\ldots,\Delta\theta_n)$ represent the misalignment errors, the thicknesses, and the designed angles of the fast axis azimuths, respectively, with respect to those of the first waveplate; and $\mathbf{J}(\delta_i,\theta_i)$ is the Jones matrix of the ith waveplate calculated by Eqs. (4) or (6).

The matrix $\mathbf{U}$ is unitary, and the relations of its elements are

$$u_{22}=u_{11}^*,\qquad u_{21}=-u_{12}^*. \tag{8}$$

By using the matrix set $\{\boldsymbol{\sigma}_0,\boldsymbol{\sigma}_1,\boldsymbol{\sigma}_2,\boldsymbol{\sigma}_3\}$, the matrix $\mathbf{U}$ can be rewritten as

$$\mathbf{U}=l_0\boldsymbol{\sigma}_0+l_1\boldsymbol{\sigma}_1+l_2\boldsymbol{\sigma}_2+l_3\boldsymbol{\sigma}_3. \tag{9}$$

Generally, l_3 will not be zero; in other words, $\boldsymbol{\sigma}_3$ will not disappear in the Jones matrix of the composite waveplate; thus the effect of a composite waveplate on the polarized light cannot be treated as that of a pure waveplate. In fact, it has been proven in [19] that any optical system which contains any number of waveplates and rotators can be optically equivalent to a cascaded system containing a pure waveplate and a rotator. Therefore, the Jones matrix of the composite waveplate can be written as

$$\mathbf{U}=\mathbf{R}(-\rho_e)\mathbf{R}(\theta_e)\mathbf{J}(\delta_e)\mathbf{R}(-\theta_e)=\mathbf{R}(-\rho_e)\mathbf{J}(\delta_e,\theta_e), \tag{10}$$

where (δ_e,θ_e) are the equivalent retardance and the equivalent fast axis azimuth, respectively, of the composite waveplate; and ρ_e is the resulting rotary angle.

Combining Eq. (7) and (10), we can derive the expressions of the equivalent parameters of the composite waveplate, shown as

$$\delta_e(\boldsymbol{\alpha},\mathbf{d},\boldsymbol{\Delta\theta},\theta_1)=2\tan^{-1}\left(\sqrt{\frac{\mathrm{Im}^2(u_{11})+\mathrm{Im}^2(u_{12})}{\mathrm{Re}^2(u_{11})+\mathrm{Re}^2(u_{12})}}\right), \tag{11a}$$

$$\theta_e(\boldsymbol{\alpha},\mathbf{d},\boldsymbol{\Delta\theta},\theta_1)=\frac{1}{2}\tan^{-1}\left(\frac{\mathrm{Re}(u_{11})\mathrm{Im}(u_{12})+\mathrm{Im}(u_{11})\mathrm{Re}(u_{12})}{\mathrm{Re}(u_{11})\mathrm{Im}(u_{11})-\mathrm{Re}(u_{12})\mathrm{Im}(u_{12})}\right), \tag{11b}$$

$$\rho_e(\boldsymbol{\alpha},\mathbf{d},\boldsymbol{\Delta\theta},\theta_1)=\tan^{-1}\left(\frac{\mathrm{Re}(u_{12})}{\mathrm{Re}(u_{11})}\right). \tag{11c}$$

Combining Eq. (7) and (9), we can obtain

$$u_{11}=l_0+l_1,\qquad u_{12}=l_2-il_3,$$
$$u_{21}=l_2+il_3,\qquad u_{22}=l_0-l_1. \tag{12}$$

Furthermore, considering that the matrix $\mathbf{U}$ is unitary as shown in Eq. (8), the following equations can be derived:

$$\mathrm{Re}(u_{11})=\mathrm{Re}(u_{22})=l_0,\quad \mathrm{Im}(u_{11})=-\mathrm{Im}(u_{22})=-il_1,$$
$$\mathrm{Re}(u_{12})=-\mathrm{Re}(u_{21})=-il_3,\quad \mathrm{Im}(u_{12})=\mathrm{Im}(u_{21})=-il_2. \tag{13}$$

Therefore, Eq. (11) can also be written as

$$\delta_e(\boldsymbol{\alpha},\mathbf{d},\boldsymbol{\Delta\theta},\theta_1)=2\tan^{-1}\left(\sqrt{\frac{-l_1^2-l_2^2}{l_0^2-l_3^2}}\right), \tag{14a}$$

$$\theta_e(\boldsymbol{\alpha}, \mathbf{d}, \boldsymbol{\Delta\theta}, \theta_1) = \frac{1}{2}\tan^{-1}\left(\frac{l_0 l_2 - i l_1 l_3}{l_0 l_1 + i l_2 l_3}\right), \tag{14b}$$

$$\rho_e(\boldsymbol{\alpha}, \mathbf{d}, \boldsymbol{\Delta\theta}, \theta_1) = \tan^{-1}\left(\frac{-i l_3}{l_0}\right). \tag{14c}$$

Since the retardances and the fast axis azimuths of the single waveplates can be determined by $(\boldsymbol{\alpha}, \mathbf{d}, \boldsymbol{\Delta\theta}, \theta_1)$, the equivalent parameters of the composite waveplate are functions of $(\boldsymbol{\alpha}, \mathbf{d}, \Delta\boldsymbol{\theta}, \theta_1)$, as shown in Eqs. (11) or (14). Equations (11a)–(11c) or (14a)–(14c) describe the relationships between the equivalent parameters and the misalignment errors, as well as the thicknesses and fast axis azimuths of the composite waveplate.

In the previously discussed model, we assume that the light propagates in a direction perpendicular to the optical axis (i.e., the extraordinary direction of the crystal) of the waveplate, and the birefringent crystal exhibits only a linear birefringence property. However, the optical axis of the waveplate will always have a small tilt angle with respect to the light propagation direction due to imperfect fabrications or improper mounting conditions. In these practical cases, some birefringent crystals such as quartz exhibit not only a linear birefringence property but also a circular birefringence property (i.e., optical activity) [21]. Here, we use a simple model to account for the optical activity, in which we ignore the effect of the small tilt angle of the optical axis on the retardance. As shown in Fig. 1, an angle ε_i is formed by the intersection of the optical axis of the ith waveplate and the x-o-y plane. The optical activity causes an additional rotary angle which can be calculated by using

$$\rho = \sum_i \gamma_i \cdot d_i \sin \varepsilon_i, \tag{15}$$

where γ_i and d_i are the optical activity and the thickness, respectively, of the ith waveplate. Then, the total rotary angle of the composite waveplate is modified by

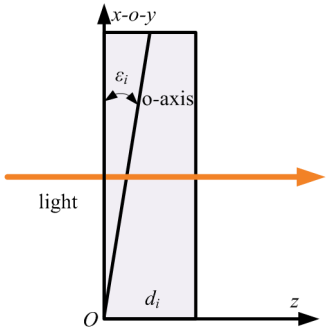

Fig. 1. Scheme of the optical axis (o axis) tilt of the waveplate in the optical path. Light propagates with the z axis, and the o axis intersects at an angle ε with the x-o-y plane.

$$\rho_e' = \rho + \rho_e, \tag{16}$$

where ρ_e and ρ can be calculated by Eqs. (14c) and (15), respectively.

B. Inverse Extraction of Misalignment Errors

We have constructed a forward model of the composite waveplate through a mathematical derivation in the previous subsection. In general, Eqs. (11) or (14) can be very complex, and the relationship between the misalignment errors and the equivalent parameters of composite waveplates is highly nonlinear. Thus, the extraction of the misalignment errors is a typically ill-posed inverse problem. Here we propose an approach using the Levenberg–Marquardt (LM) algorithm to solve this inverse problem [22,23]. Given the initial values of the misalignment errors, the LM algorithm solves the inverse problem in an iterative fitting scheme, in which the misalignment errors are adjusted until the simulated spectra of the equivalent parameters fit the input spectra. A flowchart of the misalignment error extraction with the LM algorithm is shown in Fig. 2. The optimization problem can be formulated as

$$(\boldsymbol{\alpha}') = \arg\min_{(\boldsymbol{\alpha})} \sum_{j=1}^{N} [\Gamma_{es}(\lambda_j) - \Gamma_{ei}(\lambda_j)]^2, \tag{17}$$

where $(\boldsymbol{\alpha}')$ denotes the optimized misalignment errors (i.e., the extracted misalignment errors); $\Gamma_{es}(\lambda_j)$ and $\Gamma_{ei}(\lambda_j)$ denote the theoretical simulated equivalent parameter spectra [i.e., $\delta_{es}(\lambda_j)$, $\theta_{es}(\lambda_j)$, or $\rho_{es}(\lambda_j)$] and the input equivalent parameter spectra [i.e., $\delta_{ei}(\lambda_j)$, $\theta_{ei}(\lambda_j)$, or $\rho_{ei}(\lambda_j)$], respectively; and N denotes the total number of utilized wavelengths.

3. Numerical Example

A. Triplate

To understand and analyze the equivalent model of the composite waveplate, here we give a three-in-one composite waveplate called a triplate as an example in this paper. Figure 3 shows the schematic diagram of the triplate. The fast axis azimuths and the retardances of the three individual single waveplates are expressed as $(\theta_1, \theta_2, \theta_3)$ and $(\delta_1, \delta_2, \delta_3)$, respectively, and the angular misalignment errors of the second and third single waveplate with respect to the first single waveplate are expressed as (α_2, α_3). The relations between the fast axis azimuths of the individual single waveplates are $\theta_2 = \theta_1 + 90° + \alpha_2$ and $\theta_3 = \theta_1 + 90° + \alpha_3$. We use the superscripts b and t to represent the biplate and triplate in the following derivation.

According to Eqs. (7) and (9), the characteristic Jones matrix of the triplate can be calculated by using

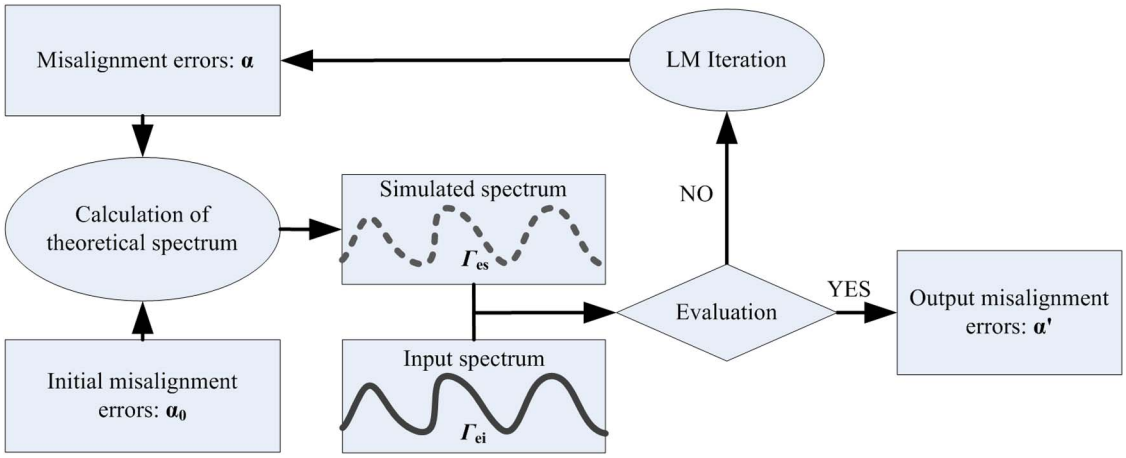

Fig. 2. Flowchart of the extraction of misalignment errors using the LM algorithm.

$$\begin{aligned}\mathbf{U}^{(t)} &= \mathbf{J}(\delta_3,\theta_3)\mathbf{J}(\delta_2,\theta_2)\mathbf{J}(\delta_1,\theta_1)\\ &= l_0^{(t)}\boldsymbol{\sigma}_0 + l_1^{(t)}\boldsymbol{\sigma}_1 + l_2^{(t)}\boldsymbol{\sigma}_2 + l_3^{(t)}\boldsymbol{\sigma}_3. \end{aligned} \tag{18}$$

The coefficients $l_0^{(t)}, l_1^{(t)}, l_2^{(t)}$, and $l_3^{(t)}$ can be obtained by

$$\begin{aligned}
l_0^{(t)} &= l_0^{(b)}\cos\frac{\delta_3}{2} + i\sin\frac{\delta_3}{2}(l_1^{(b)}\cos 2\theta_3 + l_2^{(b)}\sin 2\theta_3),\\
l_1^{(t)} &= l_1^{(b)}\cos\frac{\delta_3}{2} + i\sin\frac{\delta_3}{2}(l_0^{(b)}\cos 2\theta_3 + il_3^{(b)}\sin 2\theta_3),\\
l_2^{(t)} &= l_2^{(b)}\cos\frac{\delta_3}{2} + i\sin\frac{\delta_3}{2}(-il_3^{(b)}\cos 2\theta_3 + l_0^{(b)}\sin 2\theta_3),\\
l_3^{(t)} &= l_3^{(b)}\cos\frac{\delta_3}{2} + \sin\frac{\delta_3}{2}(-l_2^{(b)}\cos 2\theta_3 + l_1^{(b)}\sin 2\theta_3),
\end{aligned} \tag{19}$$

where $l_0^{(b)}, l_1^{(b)}, l_2^{(b)}$, and $l_3^{(b)}$ are the coefficients of the biplate combining the first and second single waveplates of the triplate and can be calculated by using

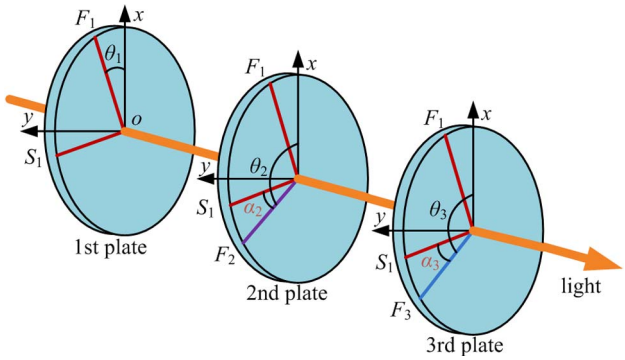

Fig. 3. Schematic of the triplate. Relations of the fast axis azimuths of single waveplates are $\theta_2 = \theta_1 + 90° + \alpha_1$ and $\theta_3 = \theta_1 + 90° + \alpha_2$. S_1 is the slow axis of the first waveplate, and (F_i, θ_i) $(i = 1, 2, 3)$ denotes the fast axes and their azimuths relative to the x axis. α_1 and α_2 denote the angular misalignment errors of the second and third waveplates, respectively, in relation to the first waveplate.

$$\begin{aligned}
l_0^{(b)} &= \cos\frac{\delta_2}{2}\cos\frac{\delta_1}{2} - \sin\frac{\delta_2}{2}\sin\frac{\delta_1}{2}\cos(2\theta_2 - 2\theta_1),\\
l_1^{(b)} &= i\left(\cos\frac{\delta_2}{2}\sin\frac{\delta_1}{2}\cos 2\theta_1 + \sin\frac{\delta_2}{2}\cos\frac{\delta_1}{2}\cos 2\theta_2\right),\\
l_2^{(b)} &= i\left(\cos\frac{\delta_2}{2}\sin\frac{\delta_1}{2}\sin 2\theta_1 + \sin\frac{\delta_2}{2}\cos\frac{\delta_1}{2}\sin 2\theta_2\right),\\
l_3^{(b)} &= -i\sin\frac{\delta_2}{2}\sin\frac{\delta_1}{2}\sin(2\theta_2 - 2\theta_1).
\end{aligned} \tag{20}$$

Finally, we obtain the expressions of the equivalent parameters of the triplate by inserting Eqs. (19) and (20) into Eq. (21):

$$\delta_e^{(t)}(\alpha_2,\alpha_3,d_1,d_2,d_3,\theta_1) = 2\tan^{-1}\left(\sqrt{\frac{-l_1^{(t)2} - l_2^{(t)2}}{l_0^{(t)2} - l_3^{(t)2}}}\right), \tag{21a}$$

$$\theta_e^{(t)}(\alpha_2,\alpha_3,d_1,d_2,d_3,\theta_1) = \frac{1}{2}\tan^{-1}\left(\frac{l_0^{(t)}l_2^{(t)} - il_1^{(t)}l_3^{(t)}}{l_0^{(t)}l_1^{(t)} + il_2^{(t)}l_3^{(t)}}\right), \tag{21b}$$

$$\rho_e^{(t)}(\alpha_2,\alpha_3,d_1,d_2,d_3,\theta_1) = \tan^{-1}\left(\frac{-il_3^{(t)}}{l_0^{(t)}}\right). \tag{21c}$$

B. Effect of the Misalignment Errors

In the following sections, we use an MgF_2–MgF_2–quartz triplate which designed as an achromatic waveplate in the wavelength range of 450 to 650 nm as an example to show the numerical simulations. A schematic diagram of the triplate is shown in Fig. 3. In the triplate, the first and the second single waveplates are made from MgF_2, and the third single waveplate is made from quartz. The thicknesses of

the three single waveplates are $d_1 = 419$ μm, $d_2 = 200$ μm, and $d_3 = 267.5$ μm, and the birefringences of quartz and MgF_2 involved in our simulations can be calculated by Sellmeier's equations [24,25]. Thus, the retardances of the three single waveplates can be calculated by Eq. (2). The fast axis azimuth of the first single waveplate is set at $\theta_1 = 0$, and the fast axis azimuths of the second and the third single waveplates are $\theta_2 = 90° + \alpha_2$ and $\theta_3 = 90° + \alpha_3$, respectively. In practice, the misalignment errors are generally less than 1°; thus we examine the effect of the misalignment errors on the equivalent parameter spectra of the triplate with the misalignment errors $(\alpha_2, \alpha_3) = (0, 0)$, (0.5°, 0.5°), and (1°, 1°). In the simulations, we assume the light propagates perpendicular to the optical axis of the waveplates, i.e., $\rho = 0$ in Eq. (15). Under these conditions, we completed the simulations by using Eqs. (19)–(21) in the visible wavelength range from 400 to 700 nm.

To clearly observe the effect of the misalignment errors on the equivalent retardance spectra, we simulated the difference between the spectrum containing misalignment errors and the ideal spectrum of the equivalent retardance [as shown in Eq. (22)] instead of the retardance spectra themselves:

$$\Delta\delta_e = \delta_e(\alpha_2, \alpha_3) - \delta_e(0, 0). \tag{22}$$

Here, $\Delta\delta_e$ is the difference between the spectrum containing misalignment errors and the ideal spectrum of the equivalent retardance, and $\delta_e(\alpha_2, \alpha_3)$ and $\delta_e(0, 0)$ refer to the equivalent retardance spectrum containing misalignment errors (α_2, α_3) and the ideal equivalent retardance spectrum, respectively.

Figure 4 shows the simulation results under different angular misalignment errors. In Fig. 4, obvious oscillations in the equivalent parameter spectra

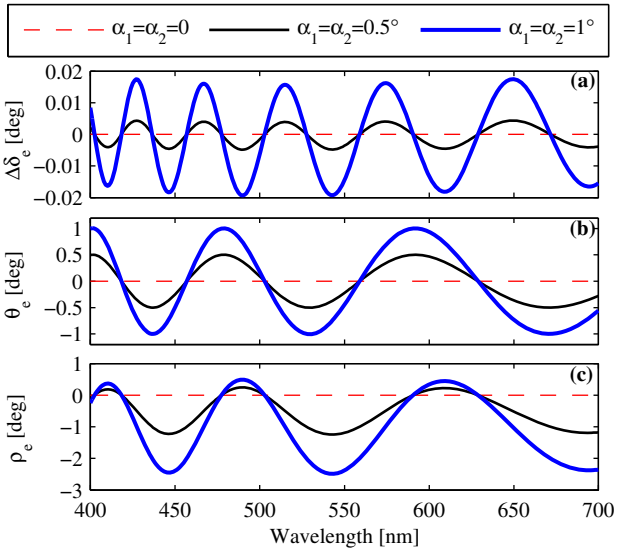

Fig. 4. Simulated oscillations in the equivalent parameter spectra of the MgF_2–MgF_2–quartz triplate with the misalignment errors $\alpha_1 = \alpha_2 = 0$, 0.5°, and 1°. (a) Differences of equivalent retardances, (b) equivalent fast axis azimuths, (c) equivalent rotary angles.

can be observed. These oscillations are assigned to the angular misalignment errors between the individual single waveplates of the triplate. The amplitudes of these oscillations change with the angular misalignment errors, and show positive correlation with the misalignment errors. Moreover, it can be seen from Fig. 4 that the oscillations in the fast axis azimuth and the rotary angle spectra are much more sensitive to the misalignment errors than those in the retardance spectra. The amplitudes of the oscillations in the fast axis azimuth and the rotary angle spectra are of the same order of magnitude as the misalignment errors, and more than 1 order larger than those in the retardance spectra. It can also be seen that the periods of the oscillations in the fast axis azimuth and the rotary angle spectra are twice as long as those in the retardance spectra, and the misalignment errors do not affect the periods of these oscillations. In fact, the periods of these oscillations are determined by the thicknesses of the waveplates and the wavelengths which have no effect on the amplitudes of the oscillations. The periods increase as the thicknesses decrease and the wavelength increases.

C. Calibration of the Misalignment Errors

From the simulation results of the previous subsection, it can be concluded that the three equivalent parameters are all sensitive to the variation of the misalignment errors in composite waveplates, and they can be theoretically chosen as the characteristic parameters for the calibration of the misalignment errors. Thus, it can be expected that the angular misalignment errors can be extracted from the oscillation curves in the equivalent parameter spectra, by performing an inverse iterative fitting procedure as shown in Eq. (17). Since the oscillations in the fast axis azimuth and the rotary angle spectra are much more sensitive to the angular misalignment errors than those in the retardance spectra, we chose the fast axis azimuth and the rotary angle as the characteristic parameters to calibrate the misalignment errors in composite waveplates. Based on these considerations, we further performed the simulations concerning the inverse extraction of the angular misalignment errors from the oscillation curves of the fast axis azimuth and the rotary angle spectra. To imitate practical measurement oscillation curves of the fast axis azimuth and the rotary angle, Gaussian noise is added to the simulated oscillation curves (as shown in Fig. 5). The expected value and the standard deviation of the Gaussian noise are set as $[\mu = 0,\ \sigma = 0.05(\Gamma_{ei\,max} - \Gamma_{ei\,min})]$ and $[\mu = 0,\ \sigma = 0.1(\Gamma_{ei\,max} - \Gamma_{ei\,min})]$, respectively. Here, Γ_{ei} denotes the equivalent fast axis azimuth spectrum θ_e and the equivalent rotary angle spectrum ρ_e.

In the simulations, the thicknesses of the single waveplates are set at their designed values, and the fast axis azimuth of the first waveplate is set at $\theta_1 = 0$. Giving the initial values $(\alpha_2, \alpha_3) = (0, 0)$, the angular misalignment errors can be extracted

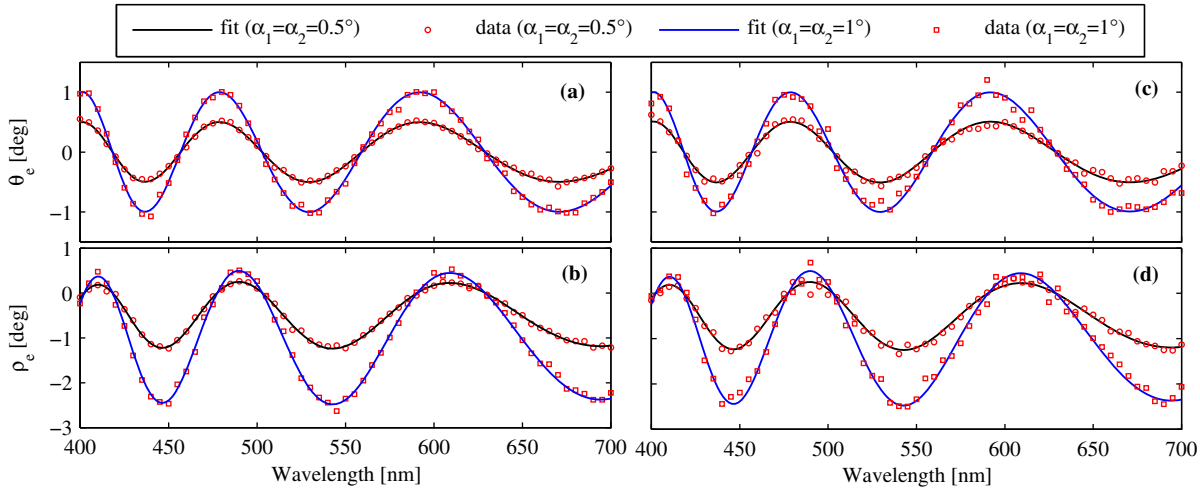

Fig. 5. Fitting results of the simulated oscillations in the equivalent fast axis azimuth and the equivalent rotary angle of the MgF_2–MgF_2–quartz triplate under different angular misalignment errors $\alpha_1 = \alpha_2 = 0.5°$ and 1°. Gaussian noise in the simulated oscillations in the fast axis azimuth and the rotary angle are as follows: (a) $\mu = 0$ and $\sigma = 0.05(\theta_{e\max} - \theta_{e\min})$, (b) $\mu = 0$ and $\sigma = 0.05(\rho_{e\max} - \rho_{e\min})$, (c) $\mu = 0$ and $\sigma = 0.1(\theta_{e\max} - \theta_{e\min})$, (d) $\mu = 0$ and $\sigma = 0.1(\rho_{e\max} - \rho_{e\min})$.

from the oscillation curves by applying the LM algorithm. Figure 5 shows the best-fit oscillation curves in the equivalent fast axis azimuth and the equivalent rotary angle as well as the simulated ones carrying Gaussian noise. The extracted results of the angular misalignment errors are presented in Table 1, where (α_2, α_3) and $(\alpha_{f2}, \alpha_{f3})$ denote the setting angular misalignment errors and the fitting misalignment errors, respectively; and $(\Delta\alpha_2, \Delta\alpha_3)$ are the differences between (α_2, α_3) and $(\alpha_{f2}, \alpha_{f3})$.

From Fig. 5 and Table 1, we can find that the best-fit curves match with the simulated curves very well, and the proportional errors of the fitting results are below 1%. Thus, the angular misalignment errors between the individual single waveplates can be accurately extracted from the oscillations in the equivalent fast axis and rotary angle spectra of the composite waveplate. The oscillations in the equivalent fast axis and rotary angle spectra can be used to minimize the angular misalignment errors (and to improve the alignment accuracy of composite waveplates). Furthermore, the proposed approach to the calibration of the misalignment errors in composite waveplates can be applied to minimize or correct the spurious oscillations in the final collected spectral data of the instruments using such waveplates.

Table 1. Extracted Results of the Angular Misalignment Errors

μ	σ	α_2 (°)	α_3 (°)	α_{f2} (°)	α_{f3} (°)	$\lvert\Delta\alpha_2/\alpha_2\rvert^a$ (%)	$\lvert\Delta\alpha_3/\alpha_3\rvert^a$ (%)
0	0.05	0.5	0.5	0.4980	0.4987	0.40	0.26
0	0.05	1.0	1.0	0.9981	0.9992	0.19	0.08
0	0.10	0.5	0.5	0.5044	0.5027	0.88	0.54
0	0.10	1.0	1.0	0.9953	0.9962	0.47	0.38

[a]Here, $|\Delta\alpha_i/\alpha_i|$ $(i = 2, 3)$ is defined as the relative error of the fitting result, and $\Delta\alpha_i = \alpha_{fi} - \alpha_i$.

4. Experiments

A. Experimental Setup

In this paper, we set up an experimental device based on the dual rotating-compensator MME principle to measure the equivalent spectral parameters of the composite waveplate in the straight-through mode [26]. This instrumentation can be described in the optical configuration $PC_{r1}SC_{r2}A$, where P and A stand for the fixed polarizer and analyzer, respectively; C_{r1} and C_{r2} refer to the first and second frequency-coupled rotating compensators, respectively; and S denotes the sample. As shown in Fig. 6, the homemade MME consists of a light source (L), a polarization state generator (PSG), a sample stage, a polarization state analyzer (PSA), and a detector (D). The PSG contains a polarizer and a rotating-compensator with the polarizer followed by the rotating-compensator, while the PSA contains an analyzer and a second rotating-compensator with the analyzer following the rotating-compensator. In the device, the light source is a deuterium (D_2) and quartz-tungsten-halogen (QTH) combined source, the polarizer and the analyzer are α-barium borate (α-BBO) Rochon prisms, the rotating-compensators are home-designed achromatic waveplates, and the detector is a commercial spectrometer. With these components used in the homemade MME, the wavelengths available are in the 210–1000 nm range, covering the spectral range of 400–700 nm used in this work. More details of the principle and the data reduction process of the dual rotating-compensator MME are given in [2]. Here, it is necessary to point out that the homemade MME has been set up with a system calibration procedure to provide all the system information including the retardances of the compensators, the azimuths of the polarized components, and the imperfections of the compensators [27].

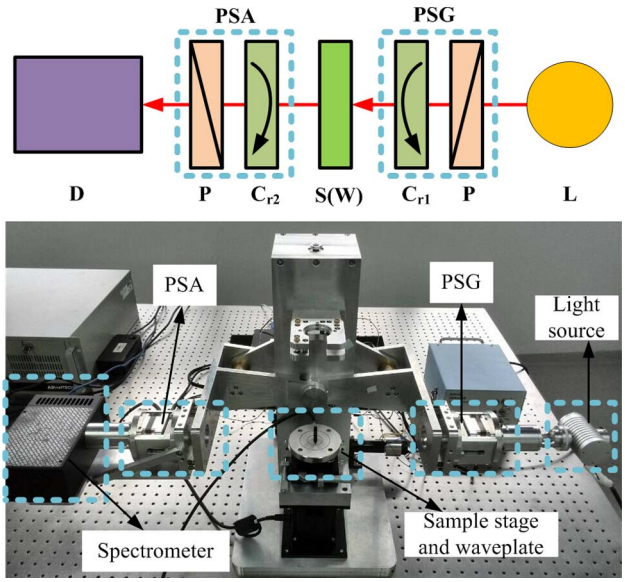

Fig. 6. Top, scheme of the dual rotating-compensator MME; bottom, homemade dual rotating-compensator MME platform.

The composite waveplate studied in this work is a commercial achromatic waveplate in the wavelength range of 450–650 nm. A schematic diagram of the composite waveplate is shown in Fig. 3, and its designed parameters have been presented in Section 3. Mounting the composite waveplate on the sample stage of the MME, we then obtain the Mueller matrix of the composite waveplate in the straight-through measurement mode. Furthermore, we can get the Jones matrix of the composite waveplate from the Mueller matrix through the relation between the Mueller and Jones matrices [28]. Finally, the equivalent spectral parameters of the composite waveplate can be calculated by using Eq. (11).

B. Experimental Results

Figure 7 shows the experimental results of the equivalent spectral parameters of the composite waveplate. As expected, obvious oscillations occur in the spectral curves of the equivalent parameter spectra, and we assign these oscillations to the angular misalignment errors between the individual single waveplates. It also can be confirmed that the amplitudes of the oscillations in the fast axis azimuth and the rotary angle spectra are much larger than those in the retardance spectrum. The experimental results show high agreement with the simulations shown in Section 3.

To extract the misalignment errors, the LM algorithm is applied to fit the experiment curves by using the equivalent model constructed in Section 2. To obtain a reasonably good fit between the experiment spectra and the calculated spectra, the thicknesses of the single waveplates as well as the fast axis azimuth of the first single waveplate are also treated as fitting parameters in the inverse extraction of the misalignment errors. The solution of the fitting parameters is achieved by minimizing a weighted mean square error function defined by

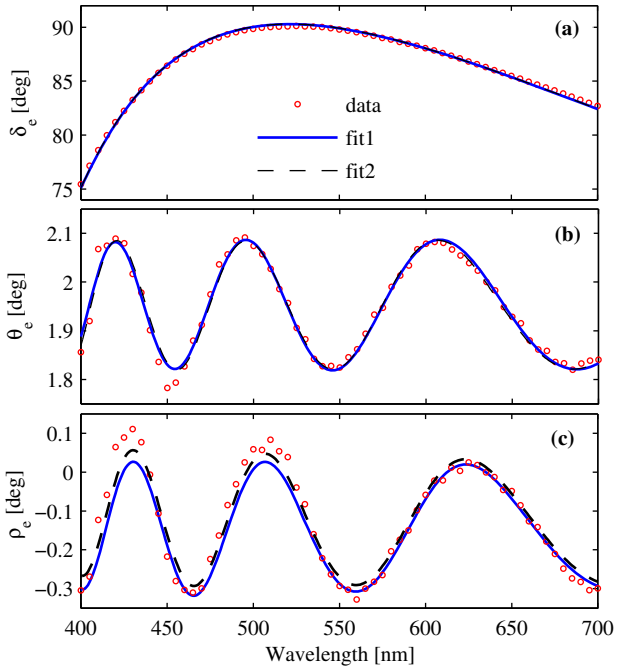

Fig. 7. Measured spectra (red open circles) of the triplate in the visible wavelength range and the best-fit spectra, using the unmodified model (blue solid line) and the modified model (black dashed line): (a) equivalent retardance $\delta_e(\lambda)$; (b) equivalent fast axis azimuth $\theta_e(\lambda)$; (c) equivalent rotary angle $\rho_e(\lambda)$.

$$\chi_r^2 = \frac{1}{3N-m}\sum_{j=1}^{N}\left[\frac{(\delta_j^m-\delta_j^c)^2}{\sigma^2(\delta_j)}+\frac{(\theta_j^m-\theta_j^c)^2}{\sigma^2(\theta_j)}+\frac{(\rho_j^m-\rho_j^c)^2}{\sigma^2(\rho_j)}\right], \tag{23}$$

where j indicates the jth spectral point from the total number N; m is the total number of the fitting parameters (δ_j^m, θ_j^m, and ρ_j^m); δ_j^c, θ_j^c, and ρ_j^c denote the measured and calculated retardance, fast axis azimuth, and rotary angle, respectively, of the triplate; and $\sigma(\delta_j)$, $\sigma(\theta_j)$, and $\sigma(\rho_j)$ are the estimated standard deviations associated with δ_j, θ_j, and ρ_j, respectively. The fitting procedure also delivers 95% confidence limits for the fitting parameters that are defined as $1.96 \times \chi_r \times C_{ii}^{1/2}$, where C_{ii} is the ith diagonal element of the fitting parameter covariance matrix [29].

The best-fit curves (fit 1) shown in Fig. 7 correspond to $d_1 = 414.51 \pm 0.139$ μm, $d_2 = 195.78 \pm 0.131$ μm, $d_3 = 267.49 \pm 0.043$ μm, $\alpha_1 = -0.017 \pm 0.0016°$, $\alpha_2 = -0.134 \pm 0.0023°$, and $\theta_1 = 2.087 \pm 0.0023°$. Compared with the designed thicknesses $d_1 = 417.5$ μm, $d_2 = 200$ μm, and $d_3 = 265$ μm, the fitting thicknesses are reasonable. The difference between the fitting and designed thicknesses is attributable to manufacturing errors. During the manufacturing process, initially the first and second individual single waveplates made from MgF_2 are aligned and cemented with their fast axes perpendicular to each other, and then they are treated as one waveplate

and aligned with its equivalent fast axis (i.e., the fast axis of the second single waveplate) parallel to that of the third single waveplate (which is made from quartz). It is obvious that the second alignment procedure is more complex and difficult than the first procedure, and this fact explains why the second misalignment error α_2 is much larger than the first misalignment error α_1 in the best-fit curves. The uncertainties of the fitting results show that the thicknesses of the first and second waveplates exhibit a relatively high correlation. This is because the first and second waveplates can be treated as a composite MgF_2 waveplate (the effective thickness of which is $d = d_1 - d_2$ when their fast axes are perpendicular to each other), and then the composite MgF_2 waveplate and the third waveplate (i.e., the quartz waveplate) form the achromatic triplate. Thus, the effective thickness $d = d_1 - d_2$ is an independent parameter in an ideal case, instead of d_1 and d_2.

It can be observed from Fig. 7 that the retardance and fast axis azimuth curves of the best-fit results match very well with the experimental results. The rotary angle curves are not as good, especially in the low wavelengths. In practice, the waveplate inevitably has a small tilt angle due to imperfect fabrication or mounting conditions; thus the optical activity of the quartz waveplate will affect the experimental results. We took the optical activity into account by using Eq. (16) to modify the model, and repeated the inverse fitting procedure. As expected, the goodness-of-fit has been improved as shown in Fig. 7. The best-fit results (fit 2) using the modified model correspond to $d_1 = 414.54 \pm 0.137$ μm, $d_2 = 195.82 \pm 0.129$ μm, $d_3 = 267.49 \pm 0.041$ μm, $\alpha_1 = -0.012 \pm 0.0015°$, $\alpha_2 = -0.132 \pm 0.0021°$, $\theta_1 = 2.086 \pm 0.0024°$, and $\varepsilon_3 = 0.13 \pm 0.0032°$, where ε_3 denotes the tilt angle of the optical axis of the third component waveplate.

5. Conclusions

Any composite waveplate can be described by three parameters: the retardance, the fast axis azimuth, and the rotary angle. All of these parameters are sensitive to the misalignment errors between the single waveplates. Thus they can be theoretically chosen as the characteristic parameters for the calibration of misalignment errors in composite waveplates. In this paper, we first derive a general analytical model to describe the relationship between the characteristic parameters and the misalignment errors in composite waveplates. Then we further propose an inverse approach to calibrate the misalignment errors in composite waveplates from the characteristic parameter spectra. Simulation results show that the characteristic parameter spectra exhibit strong oscillations when there are misalignment errors, and the oscillations show a positive correlation with the misalignment errors. Moreover, the oscillations in the fast axis azimuth and the rotary angle spectra are much more sensitive to the misalignment errors than those in the retardance spectrum. Thus, we choose the fast axis azimuth and the rotary angle as the detected characteristic parameters to calibrate the misalignment errors in composite waveplates. The relative errors are below 1% in calibrating the misalignment errors in an MgF_2–MgF_2–quartz triplate using the proposed inverse approach. An experimental device based on the dual rotating-compensator MME principle is set up to measure the characteristic parameter spectra of composite waveplates. Experimental results show high agreement with the simulations, and confirm the correctness and efficiency of the proposed approach to the calibration of the misalignment errors in composite waveplates. To deal with the small tilt angle of the optical axis in practical cases, we take into account the optical activity of the quartz waveplate and achieve an improvement for the fitting of the rotary angle spectra. This approach can be expected to improve the alignment accuracy of composite waveplates and to minimize or correct the spurious oscillations in the final collected spectral data of the instruments using such composite waveplates.

This work was funded by the National Natural Science Foundation of China (Grant Nos. 51475191, 51405172, and 91023032), the National Instrument Development Specific Project of China (Grant No. 2011YQ160002), and the Program for Changjiang Scholars and Innovative Research Team at the University of China.

References

1. A. V. Samoylov, V. S. Samoylov, A. P. Vidmachenko, and A. V. Perekhod, "Achromatic and super-achromatic zero-order waveplates," J. Quant. Spectrosc. Radiat. Transfer **88**, 319–325 (2004).
2. R. W. Collins and J. Koh, "Dual rotating-compensator multichannel ellipsometer: instrument design for real-time Mueller matrix spectroscopy of surfaces and films," J. Opt. Soc. Am. A **16**, 1997–2006 (1999).
3. J. Lee, J. Koh, and R. W. Collins, "Multichannel Mueller matrix ellipsometer for real-time spectroscopy of anisotropic surfaces and films," Opt. Lett. **25**, 1573–1575 (2000).
4. P. A. Williams, "Rotating-wave-plate Stokes polarimeter for differential group delay measurements of polarization-mode dispersion," Appl. Opt. **38**, 6508–6515 (1999).
5. D. S. Naik, C. G. Peterson, A. G. White, A. J. Berglund, and P. G. Kwiat, "Entangled state quantum cryptography: eavesdropping on the Ekert protocol," Phys. Rev. Lett. **84**, 4733–4736 (2000).
6. A. Asundi, L. Tong, and C. G. Boay, "Dynamic phase-shifting photoelasticity," Appl. Opt. **40**, 3654–3658 (2001).
7. S. Pancharatnam, "Achromatic combinations of birefringent plates. Part II. An achromatic quarter-wave plate," Proc. Indian Acad. Sci. **41A**, 137–144 (1955).
8. J. M. Beckers, "Achromatic linear retarders," Appl. Opt. **10**, 973–975 (1971).
9. P. Hariharan and P. E. Ciddor, "Broad-band superachromatic retarders and circular polarizers for the UV, visible and near infrared," J. Mod. Opt. **51**, 2315–2322 (2004).
10. J. L. Vilas, L. M. Sanchez-Brea, and E. Bernabeu, "Optimal achromatic wave retarders using two birefringent wave plates," Appl. Opt. **52**, 1892–1896 (2013).
11. E. A. Sornsin and R. A. Chipman, "Alignment and calibration of an infrared achromatic retarder using FTIR Mueller matrix spectropolarimetry," Proc. SPIE **3121**, 28–34 (1997).
12. P. Marsik and J. Humlicek, "Multi-plate misalignment artifacts in rotating-compensator ellipsometry: analysis and data treatment," Phys. Status Solidi C **5**, 1064–1067 (2008).

13. B. Boulbry, B. Bousquet, B. L. Jeune, Y. Guern, and J. Lotrian, "Polarization errors associated with zero-order achromatic quarter-wave plates in the whole visible spectral range," Opt. Express **9**, 225–235 (2001).
14. H. Dong, M. Tang, and Y. D. Gong, "Measurement errors induced by deformation of optical axes of achromatic waveplate retarders in RRFP Stokes polarimeters," Opt. Express **20**, 26649–26666 (2012).
15. H. Dai and C. X. Yan, "Measurement errors resulted from misalignment errors of the retarder in a rotating-retarder complete Stokes polarimeter," Opt. Express **22**, 11869–11883 (2014).
16. D. E. Aspnes, "Alignment of an optically active biplate compensator," Appl. Opt. **10**, 2545–2546 (1971).
17. J. Lee, P. I. Rovira, I. An, and R. W. Collins, "Alignment and calibration of the MgF_2 biplate compensator for applications in rotating-compensator multichannel ellipsometry," J. Opt. Soc. Am. A **18**, 1980–1985 (2001).
18. B. Boulbry, B. L. Jeune, F. Pellen, J. Cariou, and J. Lotrian, "Identification of error parameters and calibration of a double-crystal birefringent wave plate with a broadband spectral light source," J. Phys. D **35**, 2508–2515 (2002).
19. H. Hurwitz, Jr. and R. C. Jones, "A new calculus for the treatment of optical systems. Part II. Proof of three general equivalence theorems," J. Opt. Soc. Am. **31**, 493–499 (1941).
20. R. A. Chipman, "Polarization analysis of optical systems," Opt. Eng. **28**, 90–99 (1989).
21. T. Radhakrishnan, "The dispersion, birefringence and optical activity of quartz," Proc. Indian Acad. Sci. A **29**, 260–265 (1947).
22. J. J. More, "The Levenberg–Marquardt algorithm: implementation and theory," in *Numerical Analysis*, G. A. Watson, ed. (Springer, 1977).
23. C. W. Zhang, S. Y. Liu, T. L. Shi, and Z. R. Tang, "Improved model-based infrared reflectrometry for measuring deep trench structures," J. Opt. Soc. Am. A **26**, 2327–2335 (2009).
24. S. Chandrasekhar, "The dispersion and thermo-optic behaviour of vitreous silica," Proc. Indian Acad. Sci. A **34**, 275–282 (1951).
25. M. J. Dodge, "Refractive properties of magnesium fluoride," Appl. Opt. **23**, 1980–1985 (1984).
26. S. Y. Liu, X. G. Chen, and C. W. Zhang, "Mueller matrix polarimetry: a powerful tool for nanostructure metrology," ECS Trans. **60**, 237–242 (2014).
27. B. Johs, "Regression calibration method for rotating element ellipsometers," Thin Solid Films **234**, 395–398 (1993).
28. O. Arteaga and A. Canillas, "Analytic inversion of the Mueller–Jones polarization matrices for homogeneous media," Opt. Lett. **35**, 559–561 (2010).
29. X. G. Chen, S. Y. Liu, H. G. Gu, and C. W. Zhang, "Formulation of error propagation and estimation in grating reconstruction by a dual-rotating compensator Mueller matrix polarimeter," Thin Solid Films **571**, 653–659 (2014).